Steady and Unsteady Computation of Impeller-Stirred Reactors

Albert D. Harvey III
The Dow Chemical Company, Plaquemine, LA 70765

Stuart E. Rogers
NASA Ames Research Center, Moffett Field, CA 94035

A general computational approach is presented for numerical modeling of viscous flow in baffled, impeller-stirred-tank reactors. A multiblock, body-fitted grid structure facilitates modeling of various impeller and baffle designs, and a new procedure offers averaged velocity data from a complex 3-D CFD dataset. Impellers are modeled precisely, eliminating the need for inputting experimental velocity data for boundary conditions. The method can be used quickly to obtain extremely detailed flow computations at a fraction of the cost of computing unsteady moving grid solutions. A steady-state computational approach that neglects the relative motion between impeller and baffles yields numerical results comparably accurate to full unsteady computations for laminar flow at a fraction of the time and expense. The approximate steady-state method is used to predict power requirements of a Rushton turbine in laminar flow.

An unsteady, moving grid technique provides time-accurate solutions for the flow inside an impeller-stirred reactor with side-wall baffles. These computed results are compared with those using the approximate steady-state method and with experimental measurements. The unsteady, moving grid method uses two different initial conditions: one starting from rest and the other starting from an approximate steady-state solution obtained at the starting position of the impeller relative to the baffles. For unsteady simulations of laminar flow in stirred vessels, the final operating condition can be achieved much more efficiently if the solution obtained from the steady-state procedure is used as an approximate initial condition.

Introduction

Impeller-stirred-tank reactors are widely used in industrial applications for mixing and blending of viscous liquids for polymerization or reaction. Due to its complexity, study of the stirred tank has traditionally been an experimental effort employing such techniques as laser Doppler velocimetry (LDV) for measuring individual velocity components and laser sheet illumination (LSI) for qualitative visualization of flow patterns inside the vessel. Other experimental techniques include laser-induced fluorescence (LIF) and coherent anti-Stokes Raman spectroscopy (CARS). All these experimental techniques require a significant investment in equipment and manpower to perform and usually includes construction of a smaller scale process, since analysis of real full-size equipment is often impossible.

Another method of analysis that has become popular in the study of industrial fluid flow processes in recent years is computational fluid dynamics (CFD) and involves use of the high-speed digital computer. There has been quite a large and impressive effort in modeling stirred tanks in the last few years. The most common approach has been to measure experimentally (Fokema et al., 1994; Kresta and Wood, 1991), or provide some theoretical or analytical expression for (Ju et al., 1990) the time-averaged velocity field in the immediate vicinity of the rotating impeller, and use these data as boundary conditions for the computations. Although this method has been performed with varying degrees of success, the need

Correspondence concerning this article should be addressed to A. D. Harvey III.

to perform measurements places limitations on the computational technique as a rigorous design tool. Quite often, the time-averaged boundary conditions measured experimentally do not satisfy continuity and must be modified to obtain accurate results.

The present work presents grid generation and flow solution procedures for modeling the flow inside the impeller-stirred tank. The impellers are modeled completely, and thus no *a priori* experimental measurements are required. To simplify the problem for the purposes of validation, the flows considered in the present work are laminar, and turbulence modeling efforts are a subject of future investigations. This article discusses two different modeling techniques for the impeller stirred tank. The first is an approximate steady-state procedure that involves precise geometric modeling of the impellers and baffles, using a generalized coordinate system. The flow is solved at one impeller position in a rotating frame of reference, neglecting the relative motion between the rotating and stationary components (Harvey et al., 1995). The resulting flow is spatially averaged and compared with time-averaged experimental data.

The second method is an unsteady approach, whereby the relative motion between impellers and baffles is modeled using moving-grid techniques. Recently, a few notable unsteady computational efforts have appeared in the literature (Gosman et al., 1992; Perng and Murthy, 1992). However, a rigorous experimental validation effort has yet to appear. It is shown that for laminar flows of viscous fluids in stirred tanks, computed results using the approximate steady-state method agrees equally well with experimental results at a fraction of the cost of performing the full unsteady computations. It is concluded that the steady-state method can provide an extremely useful design tool.

A zonal, curvilinear grid procedure is employed and is applicable to complex geometries. The zonal grid construction presented in the present work is systematic and hence programmable. Thus, changes in the geometry can be easily and quickly accommodated, thus allowing for rapid analysis of multiple tank configurations. Grid zones attached to the impellers are made to rotate relative to grid zones attached to the stationary baffles. Boundaries of adjacent grid zones are specified using a two-cell zonal overlapping procedure.

The flow solver is a time-accurate incompressible Navier–Stokes solver developed by Rogers et al. (1991) and Rogers and Kwak (1988). The solver uses the artificial compressibility method of coupling the pressure and velocity fields. In an incompressible flow, the pressure does not appear explicitly in the continuity equation even though the pressure field has a direct influence on the divergence of the velocity. The artificial compressibility method involves adding a pseudo time derivative in pressure to the continuing equation that transforms the incompressible Navier–Stokes equation set into a hyperbolic set of partial differential equations. A pseudocompressibility parameter is then used to adjust the magnitude of pressure waves or disturbances that are made to propagate at a finite speed throughout the flow field. The solution procedure involves driving the pseudo-time-pressure derivative to zero, thus satisfying continuity. Centrifugal and Coriolis force terms have been added to the solver for application to rotating systems (Harvey et al., 1995). The reduced set of algebraic equations is solved using a multidirectional line-relaxation algorithm that obtains numerical solutions to the Navier–Stokes system of equations very efficiently.

In the next two sections, grid generation and Navier–Stokes solution procedures used in discretizing and solving for the incompressible flow in the general stirred tank are described. Subsequent sections include computational results using the approximate steady-state solution approach for a six-blade Rushton impeller in a baffled tank. Computed Power numbers vs. Reynolds number are compared with the theoretical work of Rushton et al. (1950).

In a final section computed velocity data using the unsteady moving-grid technique for a single 45° pitched-blade impeller is compared with experimental LDV results and with results using the approximate steady-state approach presented in Harvey et al. (1995).

Grid Generation

Single impeller construction

This section presents a generalized procedure for discretizing the flow domain inside a stirred tank. For complex geometries with many solid surfaces, such as impeller turbines, numerical grid generation can become extremely complex, but it is beyond the scope of the present work to present all of the necessary background on the subject. Thompson et al. (1985) provide an excellent reference to the fundamental concepts as well as the more advanced techniques in grid generation. Another excellent reference on numerical grid-generation techniques is that of Eiseman (1985).

Boundary-fitted coordinates are employed so that the computational grid in physical space is mapped into a uniformly spaced rectangular grid in computational space. This process serves to greatly simplify the solution process by allowing grid boundaries or surfaces to conform to the physical boundaries of the region of interest.

Usually the region inside an impeller-stirred tank is too complex to be mapped into a single computational cube. The present grid-generation scheme includes a multizone gridding procedure that facilitates accurate geometrical representations of complex impeller shapes. Multiblock grid techniques are commonly used in aerospace design applications (Holst et al., 1990; Sorenson, 1989). This is a powerful grid method that involves dividing a complex problem into a number of smaller problems or zones, each of which can be properly transformed into a uniform rectangular space. The zones are then patched together using a conservative zonal overlap technique for solution on the entire domain of interest. Boundaries of adjacent grid zones that are not physical boundaries of the solution domain must be updated by interior points of the adjacent zones so that flow-field information can properly propagate throughout the domain. For unsteady computations of impeller-stirred tanks certain zones are made to rotate relative to adjacent stationary grid zones. By employing the multiblock grid methodology, changes can be made to one particular aspect of the geometry without necessitating changes to the entire solution domain. Since the major portion of the grid is constructed from the boundaries of the impeller grid zones, once a new impeller construction is defined using a set of grid zones, the remainder of the grid is built systematically.

Stirred tanks are characterized by the presence of one or more rotating impellers inside a cylindrical vessel or tank,

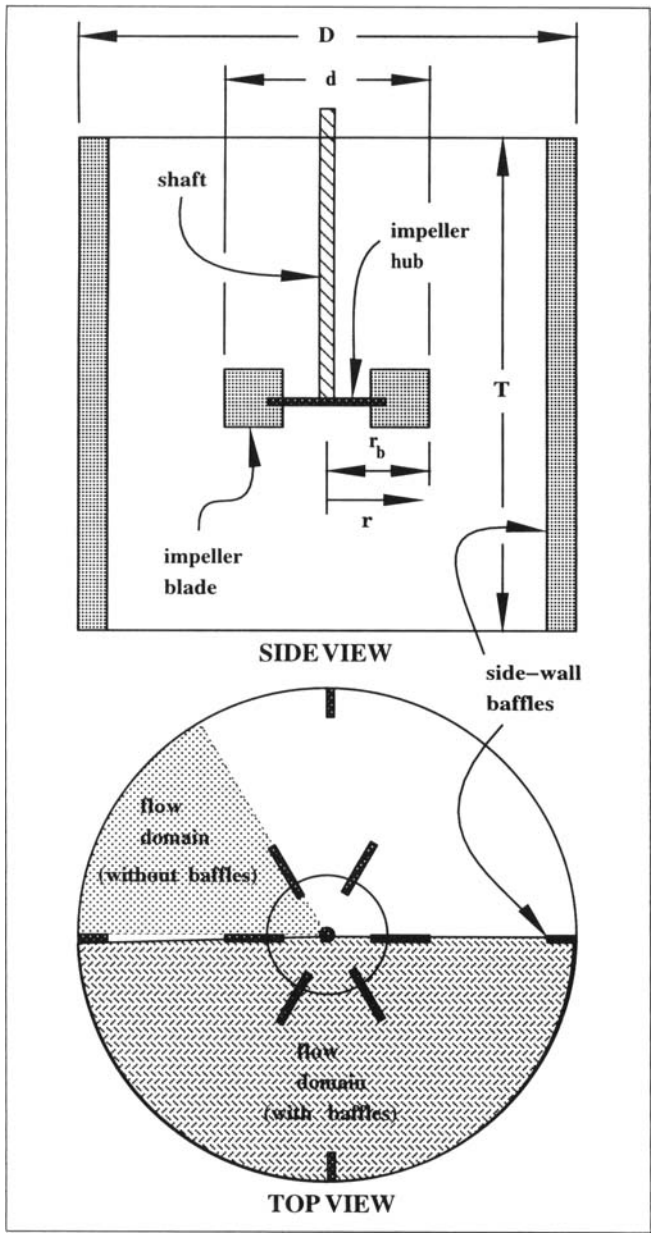

Figure 1. Typical mixing tank.

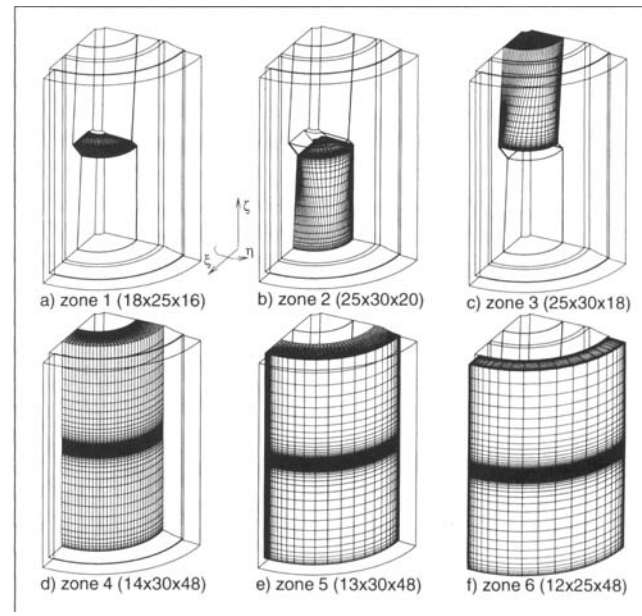

Figure 2. Zonal grid structure for single impeller configuration.

which, for the present work, are confined to rotating about a common axis. The impellers can possess any number of blades that can take on a variety of shapes and sizes. Before the grid can be constructed, the extent of the flow domain must first be determined. The amount of tank symmetry or periodicity present will, in general, depend on the number of impeller blades and side-wall baffles present. A typical stirred-tank geometry with a six-blade Rushton impeller and four rectangular side-wall baffles is illustrated in Figure 1. For this setup, one-sixth of the tank can be modeled if the baffles are excluded (or if there are six baffles present). However, one-half of the tank must be modeled with the presence of four baffles (which is quite typical).

When modeling the flow inside stirred tanks, it is often desired to change certain geometrical features of the device and then study how these changes affect such flow characteristics as circulation patterns, circulation time, impeller pumping capacity, and power requirements. This is one of the most important motivations for the present work. The multiblock grid construction allows for easy geometrical modifications. The key step in the tank-grid construction is to define the rotating-impeller region and the stationary-baffle regions with independent sets of grid zones. The remainder of the tank between these two regions is defined with additional grid zones that are designed to facilitate the relative movement between the impeller zones and baffle zones by providing an interface between moving and stationary portions of the domain.

Figure 2 illustrates the grid construction in a typical stirred tank containing a four-blade, 45° pitched-blade impeller and four rectangular stationary side-wall baffles. Due to periodicity, only one-quarter of the tank is modeled. The boundaries of each of the six grid zones are illustrated in parts (a)–(f) of the figure. At the center of the geometry is the *impeller zone* (Figure 2(a)), which describes the region between two impeller blades. Figure 2b and 2c illustrate grid zones describing the regions below and above the impeller just shown, respectively. They will be referred to as the *lower* and *upper zones*. Figure 2d and 2e illustrate what will be referred to as the *buffer zones*. They collectively discretize the region between the rotating impeller and the stationary baffles. The *inner buffer zone* of Figure 2d is fixed to the impeller and upper and lower zones. Together, these zones are made to rotate inside the *outer buffer zone*, which is fixed to the stationary *baffle zone* (Figure 2f). In addition to filling the region between impeller and baffles with grid points, the buffer zones also provide an interface between rotating and stationary components of the system. When the relative motion of the impellers and baffles is to be neglected, the inner and outer zones are combined into a single grid zone.

The computational coordinate directions ξ, η, and ζ, as drawn in Figure 2, are typical of all grid zones. The ξ-direc-

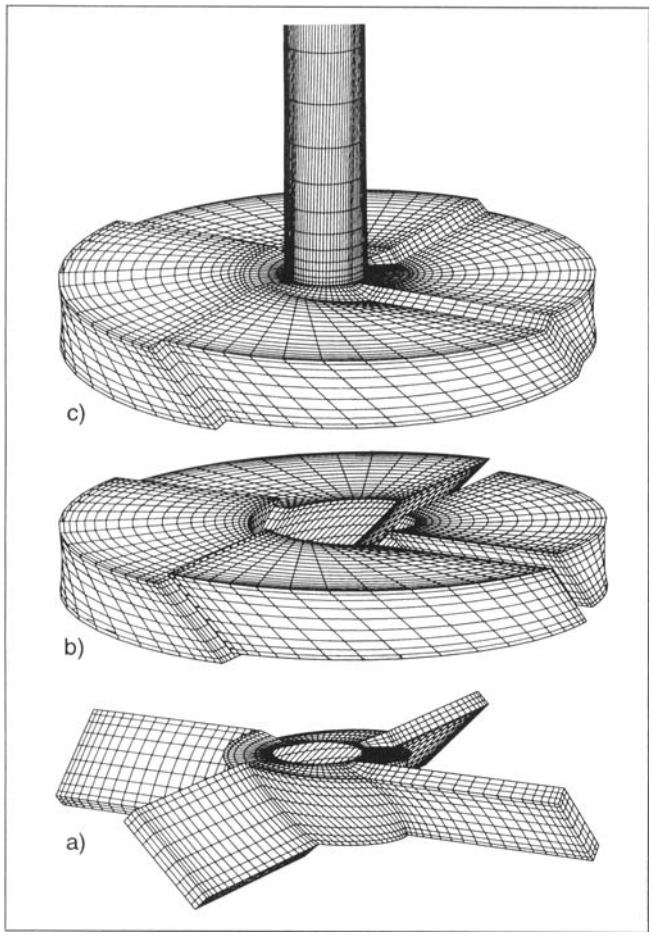

Figure 3. Zonal grid structure for pitched-blade impeller.

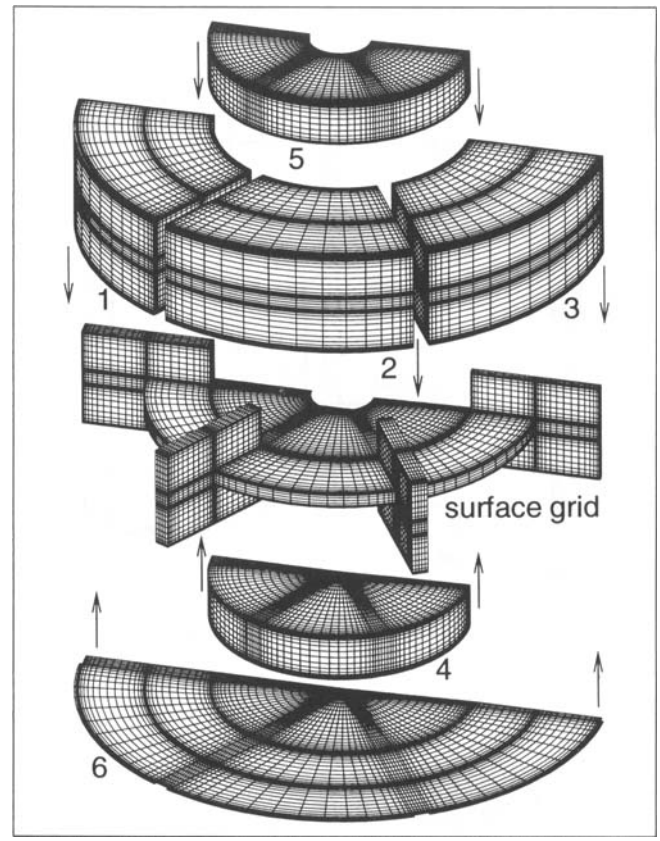

Figure 4. Zonal grid structure for Rushton disk turbine.

tion is predominantly radial, the η-direction runs circumferentially, and ζ runs in the axial direction predominately. The flow domain of Figure 2 was chosen using quarter periodicity. Quite often it is necessary to model the entire circumferential extent of the tank. Figure 3 illustrates a grid structure for the 45° pitched-blade impeller in which the entire tank is modeled. Figure 3a illustrates the surface grid of the impeller. Figure 3b illustrates the four impeller zones, while Figure 3c illustrates the complete impeller construction, including the shaft surface (which is part of the upper zone).

Using the preceding grid construction, a change in the design of the impeller requires changes only to the impeller zone assembly. The remainder of the grid (upper and lower and buffer zones) is built from the boundary surfaces of the impeller zones. Rushton-type turbines are of a construction that motivates a slightly different zonal structure near the impeller than that of Figure 3. In addition to requiring one grid zone between each adjacent pair of blades (zones 1–3 of Figure 4), two additional zones are used to define the hub region. A five-block assembly of zones is shown in Figure 4 that represents one-half of a six-blade Rushton turbine. In Figure 4, the ζ-max surface of zone 6 is also shown, which matches up with the ζ-min surfaces of zones 1–4. This grid construction would be used for the tank construction of Figure 1, where periodicity permits only half the tank to be defined.

Multiple impeller construction

When modeling multiple impellers in a mixing tank, the grid construction is essentially the same as for single impellers. For multiple impellers the assembly of grid zones consisting of the impeller zones couched between the upper and lower zones are stacked end-to-end in the axial direction. Detailed computations for the analysis of the flow in multiple-impeller-stirred tanks are presented in Harvey et al. (1996).

Boundary conditions

Each grid zone contains six faces, each of which must be supplied with boundary conditions during the solution process. All solid surfaces are assigned one of two possible no-slip boundary conditions. The first is the traditional zero-velocity, zero-pressure gradient extrapolation no-slip wall boundary condition. The second type of no-slip wall boundary is a moving-wall condition. Along with the zero-pressure gradient extrapolation the tangential-velocity magnitude is set equal to the rotational speed of the impeller multiplied by the radial distance from the axis of rotation to the wall surface, $v_t = \Omega r$. Specification of which of these two wall boundary conditions is dependent on the coordinate frame of reference chosen.

The liquid level of the tank is modeled using a z-symmetry condition (zero shear stress, $w = 0$). The boundaries of zones that are adjacent to other grid zones as well as the circumfer-

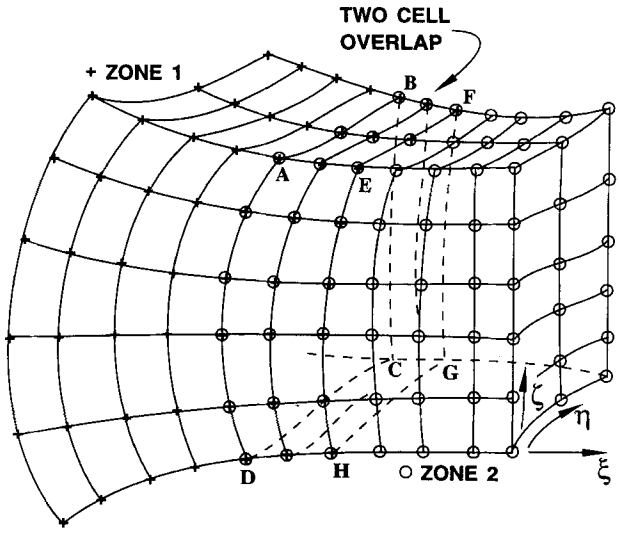

Figure 5. Zonal overlapping technique.

ential (η-faces) of the periodic zones are discussed in the next section.

Treatment of zonal interfaces

A numerical solution in the entire flow domain is obtained by an iterative procedure performed on each individual grid zone successively. As mentioned previously, the six faces of each grid zone must be supplied with boundary conditions. Faces of zones adjacent to faces of other zones are treated using a grid overlapping procedure that is illustrated in Figure 5. In this figure, two grid zones are shown. Zone 1, with grid points denoted by crosses, overlaps into zone 2, with grid points denoted by circles. For the case of Figure 5, the boundary plane *ABCD* of zone 2 is specified by flow-field values at the interior plane *ABCD* of zone 1. Likewise, the boundary plane *EFGH* of zone 1 is updated using the corresponding interior plane of zone 2.

Figure 5 illustrates the simplest block-interfacing scenario, in which all points in a zone match one-to-one with points in the adjacent zone. For this special case, dependent variable update is by direct injection of flow-field values from the interior of one zone to the boundary of another. This turns out to be a special case of a more general scenario where interpolation of surrounding points is required. Holst et al. (1990), illustrates an example in which adjacent zones match two-to-one where every other point in one zone match directly to each point in the neighboring zone. More general block-interfacing procedures are a little more involved, but implementation is straightforward. Examples can be found in Rai (1987).

Periodic boundary conditions for the circumferential η-faces of the upper and lower zones, buffer zones, and outer zone of Figures 2–4 are also supplied using the overlapping technique. Each grid point in the periodic plane is exactly one period apart from the corresponding grid point in the other periodic plane. As in Figure 5, these faces are made to overlap by two cells into the next period of the domain. Even though the matching points are not in the same physical location, the pressure as well as the *radial* and *tangential* components of the velocity are equal and can be transferred from one periodic plane to the other.

Relative grid motion

The interface between the moving and stationary zones is updated in exactly the same manner as interfaces between two stationary zones or an interface between two moving zones. The only difference is that the point-to-point mapping at the overlap on the moving interface will differ in time. Figure 6 illustrates a ζ-constant grid surface that cuts through the center of the impeller of Figure 2a. The circumferential faces of the interface grid zones are supplied as periodic boundary conditions. At each successive time after the initial condition, $t_o + n\Delta t$, the rotating zones rotate by an increment $\Omega\Delta t$. Due to the uniform η-spacing at the zonal interfaces, grid points in the inner interface zone are able to match up with the closest neighboring grid points in the outer interface zone.

As the grid rotates through its first period, less and less of the moving grid interface matches up with its stationary counterpart. More and more of the grid moves on to the next period of the periodic flow. These points are updated using the periodic overlapping technique described earlier, where the radial and tangential components of the velocity are conserved across the periodic interface.

Data Analysis

Quite often, when performing computations using hundreds of thousands of grid points, a large amount of data is generated. Extracting information useful in making reactor design decisions is not a trivial task. Harvey et al. (1995, 1996) measured the time-average velocity in a constant θ-plane inside the stirred tank for single- and multiple-impeller configurations, respectively. In order to compare the numerical results to these measurements, a circumferential or θ-averaging procedure is performed on the computed three-dimensional velocity field. This interpolation procedure is shown graphically in Figure 7. The computational grid is composed of a network of body-fitted grid zones that conform to the solid surfaces of the tank components, and is nonuniform and nonplanar. To obtain a time-averaged velocity distribution, a uniform, planar interpolation mesh is constructed in a constant θ-plane intersecting the computational domain at a specified location. The computed velocity from the computational grid is then interpolated to the uniform interpolation grid.

When the relative motion between impellers and baffles is neglected, the approximate steady-state solution is spatially averaged in the circumferential direction, resulting in a single θ-plane of data. At each grid point in the interpolation grid, a θ-constant arc is projected through the nonuniform computational grid. At discrete, evenly spaced locations along each arc, the velocity is interpolated from the computational grid and averaged to yield a θ-averaged velocity value at the corresponding grid point on the interpolation grid. The θ-averaged velocity field obtained using this averaging procedure has been shown to agree well with time-averaged velocity data obtained using LDV (Harvey et al., 1995, 1996) and is equivalent to a time-averaging procedure when the baffles are removed.

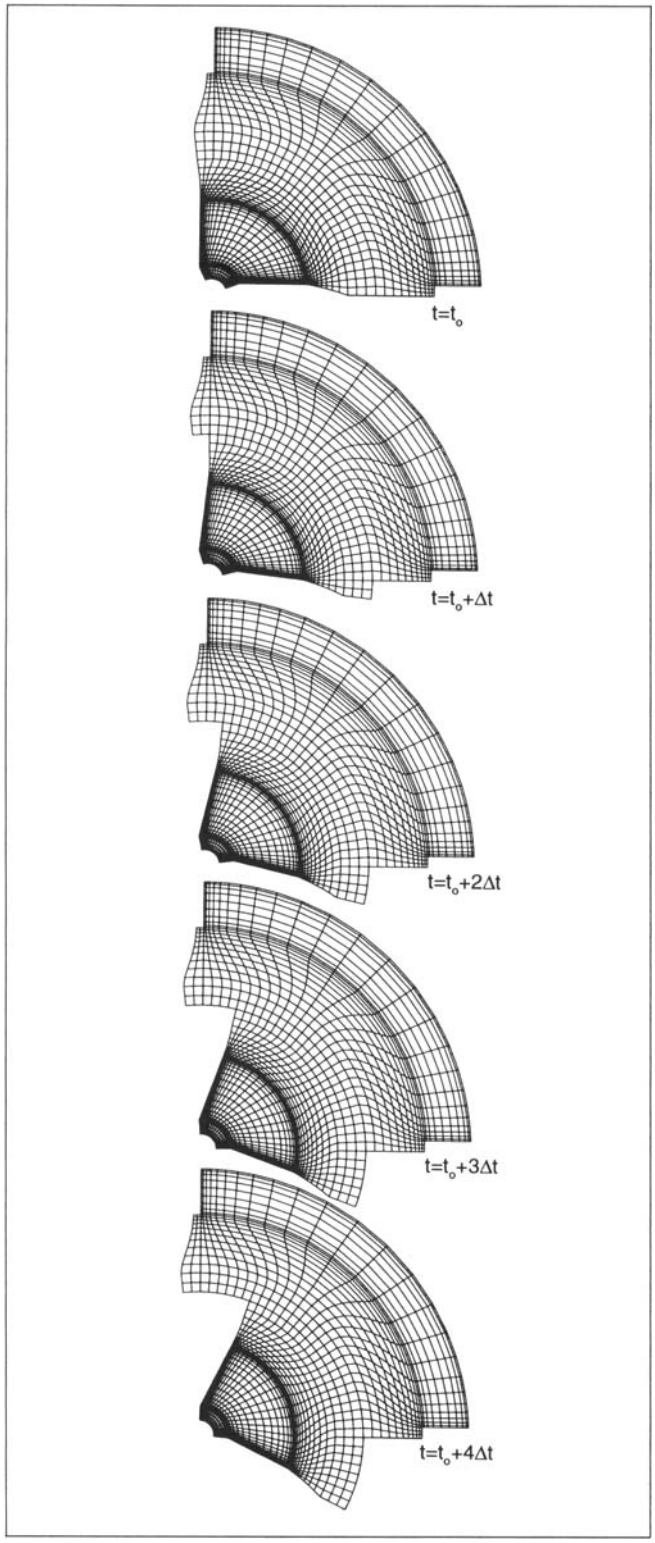

Figure 6. Moving grid technique.

When performing unsteady, moving-grid computations of stirred tanks, a three-dimensional velocity field exists at each time step in the calculations. All data sets for one period of impeller rotation, each representing a single time interval, must be interpolated to the common θ-plane. Since the grid and impellers rotate relative to the baffles, the interpolation

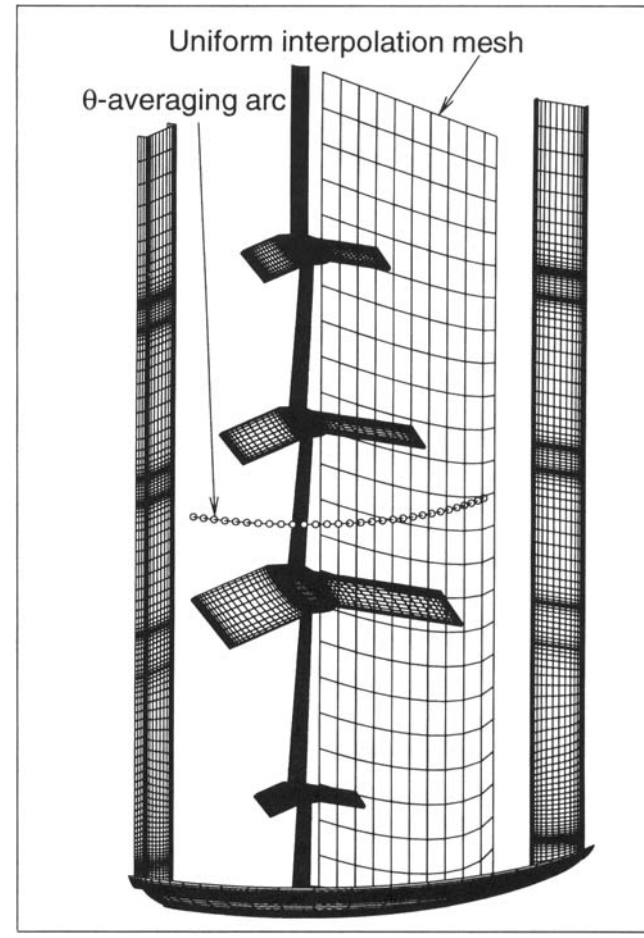

Figure 7. Three-dimensional interpolation of data onto a uniform grid.

mesh will intersect the impeller stack at a different location at each time increment. This four-dimensional interpolation procedure is not a trivial task and constitutes an additional complexity in performing unsteady calculations of impeller-stirred tanks.

Governing Equations

The time-dependent, incompressible Navier–Stokes equations can be written as a single-vector equation in a generalized coordinate system in the following standard fashion:

$$\frac{\partial \boldsymbol{Q}}{\partial t}+\frac{\partial}{\partial \xi}(\boldsymbol{E}-\boldsymbol{E}_v)+\frac{\partial}{\partial \eta}(\boldsymbol{F}-\boldsymbol{F}_v)+\frac{\partial}{\partial \zeta}(\boldsymbol{G}-\boldsymbol{G}_v)+\boldsymbol{S}_{\text{cen}}+\boldsymbol{S}_{\text{cor}}=0, \qquad (1)$$

where the inviscid fluxes in the transformed curvilinear coordinate system are written as

$$\boldsymbol{Q}=\frac{1}{J}\begin{bmatrix}0\\u\\v\\w\end{bmatrix}, \qquad \boldsymbol{H}=\frac{1}{J}\begin{bmatrix}\beta U\\u(\kappa_t+U)+\kappa_x p\\v(\kappa_t+U)+\kappa_y p\\w(\kappa_t+U)+\kappa_z p\end{bmatrix},$$

the contravariant velocities are given by

$$U = \kappa_x u + \kappa_y v + \kappa_z w.$$

In the preceding expressions, β is the pseudocompressibility parameter, and the generic inviscid flux, $\boldsymbol{H} = \boldsymbol{E}$, $\boldsymbol{F}$ and $\boldsymbol{G}$, when the generic metric terms, $\kappa = \xi$, η, and ζ, respectively. The coordinate transformation and derivation of the metric quantities are provided in the Appendix. The three viscous flux vectors, $\boldsymbol{E}_v$, $\boldsymbol{F}_v$ and $\boldsymbol{G}_v$, are written as a single generic flux vector $\boldsymbol{H}_v$, using conventional cyclic index notation in the following manner

$$\boldsymbol{H}_v = \frac{1}{J}\left(\frac{1}{Re_t}\right) \times \begin{bmatrix} 0 \\ (\nabla\xi_i\cdot\nabla\xi_i)\dfrac{\partial u}{\partial \xi_i} + (\nabla\xi_i\cdot\nabla\xi_j)\dfrac{\partial u}{\partial \xi_j} + (\nabla\xi_i\cdot\nabla\xi_k)\dfrac{\partial u}{\partial \xi_k} \\ (\nabla\xi_i\cdot\nabla\xi_i)\dfrac{\partial v}{\partial \xi_i} + (\nabla\xi_i\cdot\nabla\xi_j)\dfrac{\partial v}{\partial \xi_j} + (\nabla\xi_i\cdot\nabla\xi_k)\dfrac{\partial v}{\partial \xi_k} \\ (\nabla\xi_i\cdot\nabla\xi_i)\dfrac{\partial w}{\partial \xi_i} + (\nabla\xi_i\cdot\nabla\xi_j)\dfrac{\partial w}{\partial \xi_j} + (\nabla\xi_i\cdot\nabla\xi_k)\dfrac{\partial w}{\partial \xi_k} \end{bmatrix}.$$

Where $\boldsymbol{E}_v$, $\boldsymbol{F}_v$, and $\boldsymbol{G}_v$ are obtained when $i = 1, 2, 3$, respectively. These viscous fluxes were derived assuming a constant viscosity. In the present study, a laminar flow is assumed for the purpose of experimental validation of the methods without the presence of the added complexities of turbulence modeling. However, this assumption does not reflect a limitation in the original INS3D code (Rogers et al., 1991), which facilitates a variable fluid viscosity formulation.

The centrifugal and Coriolis forces, $\boldsymbol{S}_{\text{cen}}$ and $\boldsymbol{S}_{\text{cor}}$, are only included in the formulation when the approximate steady-state solution procedure is used and a rotating frame of reference is employed (Harvey et al., 1995). These force terms are written as

$$\boldsymbol{S}_{\text{cen}} = \frac{1}{J}\begin{bmatrix} 0 & 0 & 0 & 0 \\ 0 & -(\omega_y^2+\omega_z^2) & \omega_x\omega_y & \omega_x\omega_z \\ 0 & \omega_x\omega_y & -(\omega_x^2+\omega_z^2) & \omega_y\omega_z \\ 0 & \omega_x\omega_z & \omega_y\omega_z & -(\omega_x^2+\omega_y^2) \end{bmatrix}\begin{bmatrix} 0 \\ x \\ y \\ z \end{bmatrix}$$

$$\boldsymbol{S}_{\text{cor}} = \frac{2}{J}\begin{bmatrix} 0 & 0 & 0 & 0 \\ 0 & 0 & -\omega_z & \omega_y \\ 0 & -\omega_z & 0 & -\omega_x \\ 0 & -\omega_y & \omega_x & 0 \end{bmatrix}\begin{bmatrix} p \\ u \\ v \\ w \end{bmatrix}.$$

To solve Eq. 1 numerically, a subiterative procedure is employed that introduces an additional vector term. Employing the artificial compressibility formulation, a pressure derivative is introduced into the continuity equation. In a similar manner, velocity derivatives are added to the momentum equations, and the combined vector equation is written as

$$\frac{\partial \hat{\boldsymbol{U}}}{\partial \tau} = \hat{\boldsymbol{R}}_t + \hat{\boldsymbol{R}}_{ss} = 0, \tag{2}$$

with

$$\hat{\boldsymbol{U}} = \frac{1}{J}\begin{pmatrix} p \\ u \\ v \\ w \end{pmatrix}, \qquad \hat{\boldsymbol{R}}_t = \frac{\partial \hat{\boldsymbol{Q}}}{\partial t}$$

$$\hat{\boldsymbol{R}}_{ss} = \frac{\partial}{\partial \xi}\left(\hat{\boldsymbol{E}} - \hat{\boldsymbol{E}}_v\right) + \frac{\partial}{\partial \eta}\left(\hat{\boldsymbol{F}} - \hat{\boldsymbol{F}}_v\right) + \frac{\partial}{\partial \zeta}\left(\hat{\boldsymbol{G}} - \hat{\boldsymbol{G}}_v\right) + \boldsymbol{S}_{\text{cen}} + \boldsymbol{S}_{\text{cor}},$$

where τ is a pseudo time variable independent of the real time t. Notice that the new vector of dependent variables, $\hat{\boldsymbol{U}}$, that results from the use of the pseudocompressibility method of linking the velocity and pressure field, is the same as the unsteady flux vector, $\hat{\boldsymbol{Q}}$, except for the inclusion of pressure, p. Therefore, the old dependent vector, $\hat{\boldsymbol{Q}}$, depends only on the velocity field; however, the new dependent vector, $\hat{\boldsymbol{U}}$, depends on both the velocity and pressure fields, and the pseudocompressibility method effectively couples the continuity equation with the pressure field by introducing a pressure pseudo time derivative. The numerical procedure for obtaining the solution to the unsteady Navier–Stokes equations involves driving the pseudo time derivatives of Eq. 2 to zero.

When the unsteady solution procedure is used, the centrifugal and Coriolis force terms are omitted. However, for the steady-state solution method, the terms are included to account for the rotating frame of reference, and the transient residual, $\hat{\boldsymbol{R}}_t$, is zero. Also, when performing steady-state computations, velocity components (u_r, v_r, w_r) in a frame of reference rotating about the z-axis are transformed to the fixed frame of reference (u_a, v_a, w_a) using the following transformation:

$$u_a = u_r + y\omega_z$$
$$v_a = v_r - x\omega_z$$
$$w_a = w_r.$$

When performing large-scale computations it is often advantageous to work with numbers of order unit, and all variables in Eqs. 1 are nondimensionalized with respect to a reference velocity and/or length, as described in Harvey et al. (1995). Additional details on the numerical methods can be found in Rogers et al. (1991).

Steady-State Computational Results

Rushton turbine

In this section the flow-field generated by a six-blade Rushton turbine rotating in a cylindrical tank with four equally spaced rectangular side-wall baffles is computed. A flat-bottom tank with a diameter equal to its fill height of $T = 0.15$ m was chosen. The impeller diameter, d, was set equal to $T/3$ and was positioned half-way between the liquid level and the tank bottom. Figure 1 illustrates the tank configuration. Due to symmetry the flow in one-half of the total tank was computed (cross-hatched region of Figure 1). The baffle width was set equal to $T/10$ and the turbine blade

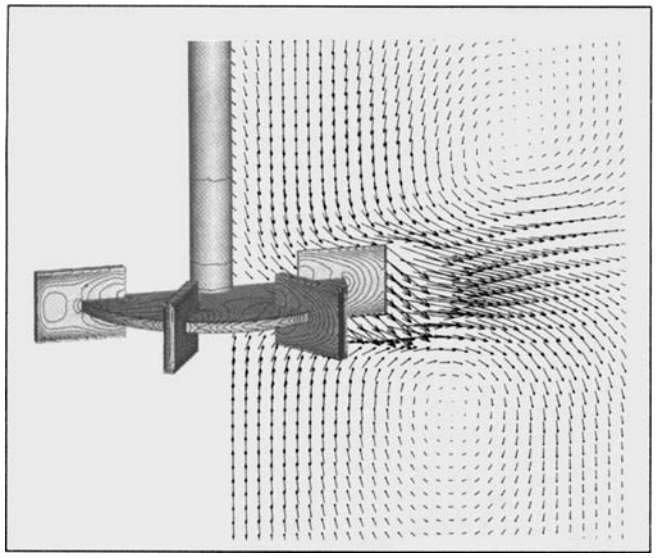

Figure 8. Computed velocity vectors and pressure contours for Rushton disk turbine.

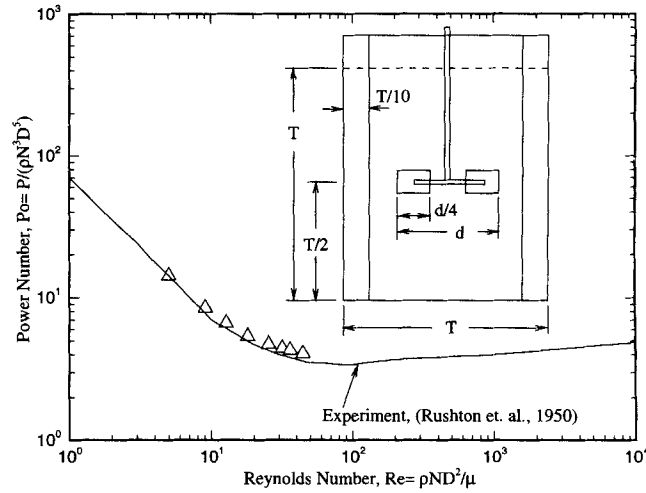

Figure 9. Reynolds number vs. Power numbers.

height was equal to $d/5$. The grid in the vicinity of the turbine is illustrated in Figure 4, and its construction was described in a previous section. The total number of grid points used for this computation was 694,815.

Figure 8 illustrates the velocity field near the impeller in a plane common to a baffle and a turbine blade. The Reynolds number for this computation is Re = 5 (100 rpm, kinematic viscosity, $\nu = 9.2 \times 10^{-4}$ m^2/s). Since the computational mesh was relatively fine and nonuniform, a clearer picture of the flow patterns is obtained by interpolating from the original computational mesh onto a comparatively coarse 40×80 plane of data, using the three-dimensional interpolation procedure described earlier.

The rotating impeller produces the familiar radial jet that deflects both up and down near the wall and then flows back radially inward toward the center of the tank. The circulating flow then reenters the turbine from above and below. Also plotted in Figure 8 are contours of constant pressure (clockwise rotation) on the turbine surfaces. Pressure is highest near the outboard blade corners on the leading side. Pressure is lowest near the center of the blade on the trailing side of the blade.

Integrating over all the surfaces of the turbine blade, the pressure, and viscous forces, the torque required to rotate the turbine can be computed:

$$\text{Torque} = \Sigma_k [\int (p + \sigma_{ij})\, dA]_k,$$

where the summation is over all the surfaces of the turbine blade, the integration is performed over the kth solid surface, and the shear stress tensor is denoted by σ_{ij}. The computed Power numbers at eight different Reynolds numbers between 5 and 44.6 are plotted in Figure 9. The semiempirical curve of Rushton et al. (1950) is also plotted in Figure 9. Very good agreement between the early work of Rushton and the computations is observed. However, as the Reynolds number increases toward a turbulent flow condition, the computational results tend to overpredict the results of Rushton.

A total of 25 megawords of memory and 6.6 hours of Cray C90 time were required to reduce the residual in the numerical solution by four orders of magnitude. At the higher Reynolds numbers, however, it became impossible to reduce the residual to this level of convergence, probably due to the use of an extremely dense grid combined with the use of the line relaxation solver and a decreasing amount of viscous dissipation in the computations.

Unsteady Computational Results

In this section the unsteady computations using the moving grid techniques are presented. The flow domain and computational grid are illustrated in Figure 2 (total grid density is 88,980 grid points). This flow was computed on this same grid (coarse grid) using the approximate steady-state procedure, and measured experimentally using LDV by Harvey et al. (1995). The rotational speed is $N = 100$ rpm, and the fluid is silicon oil with fluid density, $\rho = 1{,}049$ kg/m^3; viscosity, $\mu =$ 211 cp. These conditions correspond to a Reynolds number of $Re_t = 33.59$. The time-step, $\Delta t = 0.0055$, was chosen so that a point-to-point matching was maintained at the interface between the moving and stationary zones of Figure 6 (zones 4 and 5 of Figure 2) where the grid spacing is uniform in the tangential or η-direction.

The solution was started at the first grid position of Figure 6, with the velocity everywhere set to zero and the pressure field initialized to unity. This condition simulates the impeller-stirred tank to be initially at rest. The solution is then advanced by one time step, which initiates a rotation of the inner grid zones by an angular increment equal to $\Omega \Delta t$. This procedure is, however, not very realistic because it simulates an impeller that is initially at rest and that is instantaneously accelerated to 100 rpm. Due to the mechanical limitations of actual equipment, this condition is almost impossible to achieve in the real world. Since the impeller motor has only a finite amount of power, experimental startup of the impeller will unavoidably be accompanied by a finite rate of rotational acceleration. No attempt is made to simulate this initial ac-

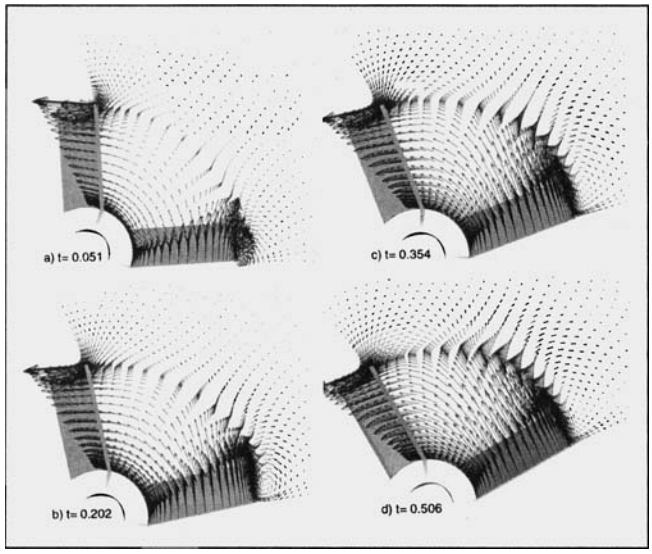

Figure 10. Computed velocity vectors for unsteady computations; quiescent initial condition (top view).

celeration in the present work, so the computations for small values of t will not represent actual startup conditions.

In practice, the final operational conditions of the stirred tank, when the fluid has everywhere accelerated to a quasi-periodic steady-state condition, is of primary interest. This flow condition can, however, take a great deal of time to achieve from a condition of a quiescent fluid, and can be quite expensive to compute. No attempt will be made in the present work to achieve the final operating condition of an impeller-stirred tank from a fluid at rest. However, for the purpose of illustration, computations are made from the quiescent fluid state for one revolution of the impeller. In the next subsection, a more tractable initial condition is employed that makes obtaining the final operating conditions more tractable from a computational standpoint.

Figure 10 illustrates velocity vectors near the impeller blade region for different values of t after startup (at $t = 0$) from quiescent conditions. Velocity on the shaft and impeller surfaces is equal to Ωr. The rotating blade initially forces fluid away from the impeller blade, then, at later times, fluid is entrained from above and below the impeller as it is forced out radially in the plane of the impeller. Note at early times that flow is actually radially inward behind the rotating impeller and radially outward in front of the impeller. This creates a blade-tip vortex motion that moves radially outward as time proceeds.

Figure 11 shows radial and axial velocity profiles computed at four different axial stations inside the tank. Tangential velocity components are shown in Figure 12. The time-averaged

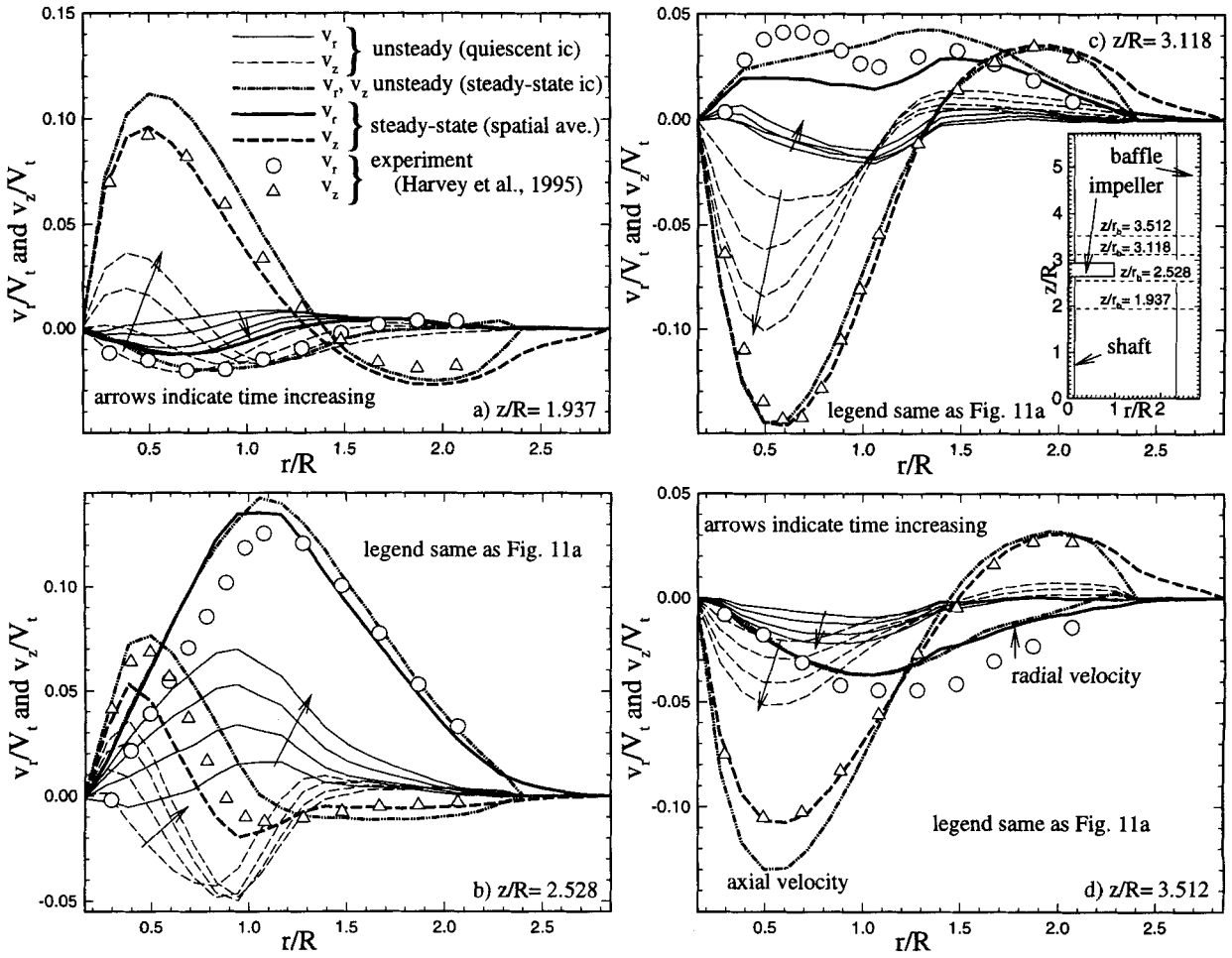

Figure 11. Comparison of computed and experimental radial and axial velocity components.

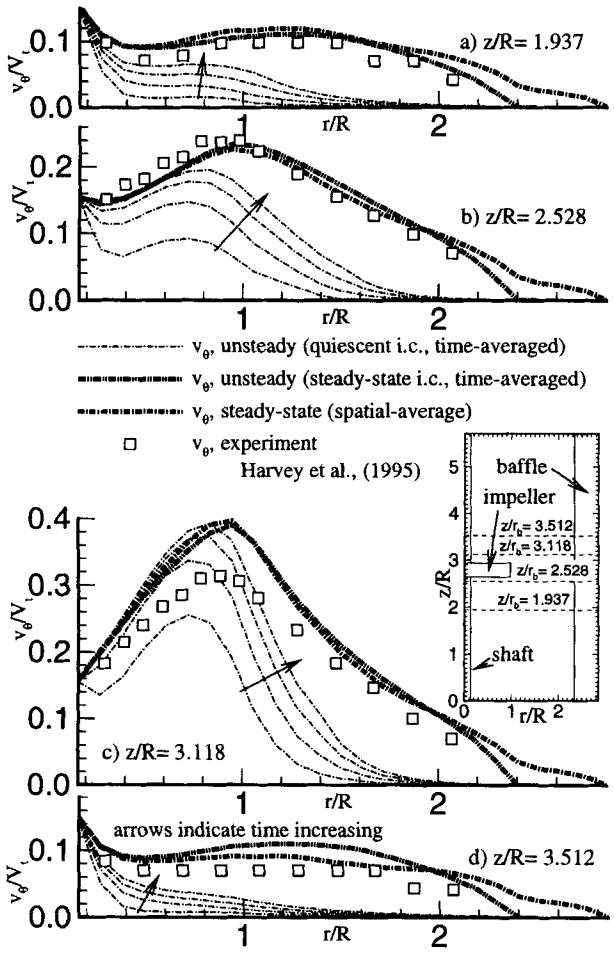

Figure 12. Comparison of computed and experimental tangential velocity components.

unsteady computations obtained from the quiescent initial condition are shown by the four thin curves (four solid curves —radial; four dashed curves—axial velocity component; four dash-dot curves—tangential). Each of these four sets of curves represents time-averaged velocity results for each of the first four quarter revolutions of the impeller. Clearly, the system has not reached a periodic steady-state condition after only one full revolution. The thicker lines show computed and spatially averaged results using the approximate steady-state method. These results compare well with the experiment, considering the less computational effort involved.

Instead of starting the unsteady computations from the quiescent fluid condition, an alternative divergence-free initial condition can be used, from which the final operating conditions can be achieved in a significantly smaller interval of time. Using the initial position of the grid, the approximate steady-state solution method is performed in a rotating frame of reference. The resulting steady-state solution approximates the flow at the instant of time the impeller is at its initial position ($t = t_o$ of Figure 6). By starting from this initial condition, the residuals associated with the time derivatives will quickly damp out and the final operating conditions of the stirred tank will be achieved much quicker than starting the computations from rest. The heavy dash-dot-dot lines of Figures 11 and 12 show the time-averaged results after one-quarter revolution of the impeller. All time-averaged results are in the θ-plane of the tank containing a side-wall baffle.

Table 1. CPU Time Comparisons

Initial Condition	CPU Fujitsu	CPU Cray C90	No. of Rev.
Quiescent	7.52	15.72	1
Steady state	2.68	5.60	0.25

Computational effort

Table 1 summarizes the CPU requirements for the unsteady computations using both the Cray C90 and a Fujitsu VP2400 for the cases of starting the calculations from both quiescent and steady-state solution initial conditions. Computational requirements for the unsteady tank computations were approximately 250 CPU s/physical time step on the Fujitsu. CPU requirements on a Cray C90 were approximately 500 CPU s/physical time step. Thus, one-quarter revolution of the impeller (27 time steps) required about 1.88 CPU hours on the Fujitsu. This equals about half the time required to compute one revolution of the impeller on the Cray C90.

To obtain the initial condition using the approximate steady-state method required about 400 iterations to reduce the maximum residual below 10^{-4} (Harvey et al., 1995) and required approximately 0.80 h of CPU time on the Fujitsu. Thus, total time spent on the unsteady solution that used the approximate steady-state solution as an initial condition (one-quarter revolution) was 2.68 hours.

The unsteady solution using the quiescent initial conditions required 7.52 h of CPU on the Fujitsu for just the first full revolution of the impeller, which was shown to be quite far from its final operating condition. In fact, reaching a periodic steady-state may take tens of revolutions of the impeller when starting from a quiescent initial condition. If it is assumed that only ten revolutions of the impeller are needed when starting from a quiescent condition to reach the level of accuracy attained by the first quarter revolution of the computation obtained using an approximate initial condition, then a 28-fold savings in computational time is realized on the Fujitsu. This clearly shows that significant savings can be realized by using the approximate steady-state solution as the initial condition in unsteady computations of laminar flow in stirred tanks.

Summary and Concluding Remarks

A multiblock grid-generation procedure is presented that is shown to be applicable to the general impeller-stirred-tank geometry. The grid-generation concepts presented can be easily programmed for almost any tank geometry. This can be done so that the user can quickly specify the various grid densities, tank and impeller dimensions, type of impeller, baffles dimensions, and most of any other aspects of the problem.

Two different solution methods are presented that can be used to solve the viscous flow in impeller-stirred tanks. The first of these methods is an approximate steady-state method that solves the impeller system at one position of the impeller relative to the side-wall baffles, neglecting relative motion al-

together. The second is an unsteady moving grid technique that obtains time-accurate solutions for the flow in a stirred tank. The impeller region of the tank is defined by a separate set of grid zones that rotate relative to the stationary baffle region.

The approximate steady-state procedure was used to compute the flow generated by a rotating Rushton disk turbine at various Reynolds numbers in the laminar regime. The computed Power numbers were shown to agree well with the semiempirical results of Rushton et al. (1950).

It is shown that for low Reynolds number flows in tanks, the steady-state solution procedure is an attractive alternative to performing full unsteady computations. When unsteady computations of viscous systems are performed, it is advantageous to use the steady-state solution procedure beforehand, to obtain an approximate initial condition. This can reduce the cost of computing the flow from a quiescent fluid condition. For high Reynolds number turbulent flows in stirred tanks, unsteady computations may be required in order to obtain realistic results. Quite possibly the steady-state solution procedure can prove valuable in analysis of higher Reynolds number flows by appropriately averaging solutions at a number of impeller positions relative to the baffles instead of a single impeller position.

Using the approximate steady-state solution procedure, parametric studies of low Reynolds number flows in stirred tanks can then be conducted efficiently. Future work using this simplified solution method will focus on how changes in geometry affect certain tank characteristics, such as flow patterns, circulation time, impeller pumping capacity, and power requirements. Other important design issues, such as scaleup, can also be easily studied with a means of quickly and systematically altering geometrical factors.

Acknowledgments

The authors would like to thank Doug Leng, Hank Kohlbrand, Jack Rhymes, and David West of The Dow Chemical Company Research and Development for their continued support of this research. Thanks also to Stewart Wood and Cassian Lee of The Dow Chemical Company for their LDV measurement work. Special thanks to Shared Gavali, Dr. Ken Miura and Joe Grisillo of Fujitsu America for providing computational resources for this research.

Literature Cited

Eiseman, P. R., "Grid Generation for Fluid Mechanics Computations," *Ann. Rev. Fluid Mech.*, **17,** 487 (1985).

Fokema, M. D., S. M. Kresta, and P. E. Wood, "Importance of Using the Correct Impeller Boundary Conditions for CFD Simulations of Stirred Tanks," *Can. J. Chem. Eng.*, **72** (1994).

Gosman, A. D., J. Y. Luo, and R. I. Issa, "Full Flow Field Computation of Mixing in Baffled Stirred Tanks," AIChE Meet., Miami Beach, FL (1992).

Harvey, A. D., C. K. Lee, and S. E. Rogers, "Steady-State Modeling and Experimental Measurement of a Baffled Pitched-Blade Impeller Stirred Tank," *AIChE J.*, **41,** 2177 (1995).

Harvey, A. D., S. P. Wood, and D. E. Leng, "Experimental and Computational Study of Multiple Impeller Flows," *Chem. Eng. Sci.*, in press (1996).

Holst, T. L., J. Flores, Ü. Kaynak, and N. M. Chaderjian, "Navier-Stokes Computations about Complex Configurations Including a Complete F-16 Aircraft," *Applied Computational Aerodynamics*, P. A. Henne, ed., AAIA, New York, p. 777 (1990).

Ju, S. Y., T. M. Mulvahill, and R. W. Pike, "Three-Dimensional Turbulent Flow in Agitated Vessels with a Nonisotropic Viscosity Turbulence Model," *Can. J. Chem. Eng.*, **68,** (1990).

Kresta, S. M., and P. E. Wood, "Prediction of the Three-Dimensional Turbulent Flow in Stirred Tanks," *AIChE J.*, **37,** 448 (1991).

Perng, C.-Y., and J. Y. Murthy, "A Moving Mesh Technique for the Simulation of Flow in Mixing Tanks," AIChE Meet., Miami Beach, FL (1992).

Rai, M. M., "Unsteady Three-Dimensional Navier Stokes Simulations of Turbine Rotor-Stator Interactions," Joint AIAA/SAE/ASME/ASEE Propulsion Conference, San Diego, CA (1987).

Rogers, S. E., D. Kwak, and C. Kiris, "Steady and Unsteady Solutions of the Incompressible Navier-Stokes Equations," *AIAA J.*, **29,** 603 (1991).

Rogers, S. E., and D. Kwak, "An Upwind Differencing Scheme for the Time Accurate Incompressible Navier-Stokes Equations," AIAA Meet., Williamsburg, VA (1988).

Rushton, J. H., E. W. Costich, and H. J. Everett, "Power Characteristics of Mixing Impellers," Parts 1 and 2, *Chem. Eng. Prog.*, **46,** 395 (1950).

Sorenson, R. L., *The 3DGRAPE Book: Theory, Users' Manual, Examples*, NASA TM 102224, NASA, Washington, DC (1989).

Thompson, J. F., Z. U. A. Warsi, and C. W. Mastin, *Numerical Grid Generation, Foundations and Applications*, Elsevier, Amsterdam (1985).

Appendix: Coordinate Transformation

A generalized functional relationship between the physical coordinates (x, y, z) in three dimensions and the computational coordinates (ξ, η, ζ) can be written as

$$\xi = \xi(x, y, z, t)$$
$$\eta = \eta(x, y, z, t)$$
$$\zeta = \zeta(x, y, z, t). \tag{A1}$$

In general, an explicit relationship between (x, y, z) and (ξ, η, ζ) is not known. Using the chain rule of the differentiation, the equations of fluid motion are transformed into computational space by replacing the derivatives in physical space with the following derivatives with respect to the computational coordinates:

$$\frac{\partial}{\partial t} = \xi_t \frac{\partial}{\partial \xi} + \eta_t \frac{\partial}{\partial \eta} + \zeta_t \frac{\partial}{\partial \zeta}$$
$$\frac{\partial}{\partial x} = \xi_x \frac{\partial}{\partial \xi} + \eta_x \frac{\partial}{\partial \eta} + \zeta_x \frac{\partial}{\partial \zeta}$$
$$\frac{\partial}{\partial y} = \xi_y \frac{\partial}{\partial \xi} + \eta_y \frac{\partial}{\partial \eta} + \zeta_y \frac{\partial}{\partial \zeta}$$
$$\frac{\partial}{\partial z} = \xi_z \frac{\partial}{\partial \xi} + \eta_z \frac{\partial}{\partial \eta} + \zeta_z \frac{\partial}{\partial \zeta}, \tag{A2}$$

where the subscripts x, y, and z refer to differentiation. It now becomes apparent that the actual functional relationship between physical and computational coordinates is not needed. What is needed are the metric quantities ξ_x, ξ_y, ξ_z, η_x, etc. The inverse relations, x_ξ, y_ξ, z_ξ, x_η, etc., are easily computed using finite differences from the computational grid points in physical space. Once these inverse relations are computed, a similarity matrix is constructed to find the necessary metric quantities. This similarity matrix is formed by expanding the total differential of each spatial coordinate in

both computational and physical space and writing the results in matrix form.

$$\begin{bmatrix} d\xi \\ d\eta \\ d\zeta \end{bmatrix} = \begin{bmatrix} \xi_x & \xi_y & \xi_z \\ \eta_x & \eta_y & \eta_z \\ \zeta_x & \zeta_y & \zeta_z \end{bmatrix} \begin{bmatrix} dx \\ dy \\ dz \end{bmatrix}, \quad \begin{bmatrix} dx \\ dy \\ dz \end{bmatrix} = \begin{bmatrix} x_\xi & x_\eta & x_\zeta \\ y_\xi & y_\eta & y_\zeta \\ z_\xi & z_\eta & z_\zeta \end{bmatrix} \begin{bmatrix} d\xi \\ d\eta \\ d\zeta \end{bmatrix}. \quad \text{(A3)}$$

Thus the following relation for the metrics is true

$$\begin{bmatrix} \xi_x & \xi_y & \xi_z \\ \eta_x & \eta_y & \eta_z \\ \zeta_x & \zeta_y & \zeta_z \end{bmatrix} = \begin{bmatrix} x_\xi & x_\eta & x_\zeta \\ y_\xi & y_\eta & y_\zeta \\ z_\xi & z_\eta & z_\zeta \end{bmatrix}^{-1}$$

$$= \begin{bmatrix} y_\eta z_\zeta - y_\zeta z_\eta & x_\zeta z_\eta - x_\eta z_\zeta & x_\eta y_\zeta - y_\eta x_\zeta \\ y_\zeta z_\xi - y_\xi z_\zeta & x_\xi z_\zeta - x_\zeta z_\xi & x_\zeta y_\xi - y_\xi y_\zeta \\ y_\xi z_\eta - y_\eta z_\xi & x_\eta z_\xi - x_\xi z_\eta & x_\xi y_\eta - x_\eta y_\xi \end{bmatrix}. \quad \text{(A4)}$$

The Jacobian of the transformation is given by

$$J = \det \frac{\partial(\xi, \eta, \zeta)}{\partial(x, y, z)} = \begin{vmatrix} \xi_x & \xi_y & \xi_z \\ \eta_x & \eta_y & \eta_z \\ \zeta_x & \zeta_y & \zeta_z \end{vmatrix}$$

$$\frac{1}{J} = x_\xi(y_\eta z_\zeta - y_\zeta z_\eta) + x_\eta(y_\zeta z_\xi - y_\xi z_\zeta) + x_\zeta(y_\xi z_\eta - y_\eta z_\xi). \quad \text{(A5)}$$

The time metrics are computed as a function of the grid velocity terms:

$$\xi_t = \xi_x \frac{\partial x}{\partial t} + \xi_y \frac{\partial y}{\partial t} + \xi_z \frac{\partial z}{\partial t}$$

$$\eta_t = \eta_x \frac{\partial x}{\partial t} + \eta_y \frac{\partial y}{\partial t} + \eta_z \frac{\partial z}{\partial t}$$

$$\zeta_t = \zeta_x \frac{\partial x}{\partial t} + \zeta_y \frac{\partial y}{\partial t} + \zeta_z \frac{\partial z}{\partial t}. \quad \text{(A6)}$$

For the case of interest in the present work, rotation is strictly about the z-axis, for which the grid-point positions in the rotating grid zones are expressed as $x = \sqrt{x_o^2 + y_o^2}\cos(\Omega t)$, $y = \sqrt{x_o^2 + y_o^2}\sin(\Omega t)$, and $z = z_o$; where (x_o, y_o, z_o) is the initial grid-point position in the Cartesian frame. After differentiating, the following results are used as exact expressions for the grid speed terms:

$$\frac{\partial x}{\partial t} = -\Omega y, \qquad \frac{\partial y}{\partial t} = \Omega x, \qquad \frac{\partial z}{\partial t} = 0.$$

Manuscript received Oct. 13, 1995, and revision received Mar. 1, 1996.